Journal of Alloys and Compounds 835 (2020) 155321

Contents lists available at ScienceDirect

Journal of Alloys and Compounds

journal homepage: http://www.elsevier.com/locate/jalcom

Construction of hierarchical $Cu_{2+1}O$@NiCoAl-layered double hydroxide nanorod arrays electrode for high-performance supercapacitor

Ying Liu [a], Xueying Cao [a], Yuxue Zhong [a], Liang Cui [b, *], Di Wei [b], Rongkun Zheng [b], Jingquan Liu [a, b, **]

[a] College of Material Science and Engineering, Institute for Graphene Applied Technology Innovation, Collaborative Innovation Centre for Marine Biomass Fibers, Materials and Textiles of Shandong Province, Qingdao University, Qingdao 266071, Shandong, China
[b] College of Material Science and Engineering, Linyi University, Linyi, 276000 Shandong, China

ARTICLE INFO

Article history:
Received 17 March 2020
Received in revised form
6 April 2020
Accepted 21 April 2020
Available online 28 April 2020

Keywords:
Copper foam
NiCoAl-Layered double hydroxide
Hierarchical structures
Core/shell nanorod arrays
Hybrid supercapacitors

ABSTRACT

Here we report the construction of a kind of electrode material with excellent capacitive performance composed of Ni, Co and Al layered double hydroxide (NiCoAl-LDH) nanosheets branched on $Cu_{2+1}O$ nanorod arrays ($Cu_{2+1}O$@NiCoAl-LDH) on copper foam current collector, which is obtained via an easy in situ chemical oxidation reaction in combination with hydrothermal method. The as-prepared $Cu_{2+1}O$@NiCoAl-LDH electrode presents observably enhanced electrochemical performance with an outstanding specific capacitance (2932 F g^{-1} at 0.75 A g^{-1}), and extraordinary cycling stability (94.27% of the initial capacitance maintained after GCD test for 6000 cycles), which are much superior to those of $Cu(OH)_2$ and $Cu_{2+1}O$@NiCo-LDH electrodes. Additionally, the $Cu_{2+1}O$@NiCoAl-LDH nanorod arrays, as a positive electrode material, can also be utilized to assemble a hybrid supercapacitor (HSC) device with an activated carbon (AC) electrode (negative electrode). The energy density of the assembled HSC device can up to 61.83 Wh kg^{-1} with a working voltage of 1.5 V, meanwhile the power density is 749.93 W kg^{-1}. Furthermore, a few Light Emitting Diode (LED) indicators with different shape combination can be lit up by the assembled HSC devices, demonstrating the practicability of the HSC device.

1. Introduction

With the rapid growth of energy consumption worldwide, more and more researchers pay their attentions to develop high-performance devices to storage energy [1–4]. Among various energy-storage devices, supercapacitor is one of the most potential one ascribing to a series of merits, such as fast charge and discharge rate, superior power density, and long cycle lifespan [5–10]. However, there is a major challenge still remained, that is how to further enhance the energy density without reducing the power density and maintain the long lifetime [1,11]. As for supercapacitors, one of the most effective strategies to enhance the energy density is developing hybrid supercapacitors (HSCs) that consist of a battery-type (pseudocapacitance) electrode and a capacitor-type (electrochemical double layer) one, which can simultaneously enhance the specific capacitance and widen the operation voltage window [12–16].

Currently, metallic layered double hydroxides (MLDHs), as a new kind of pseudocapacitive materials, have been applied in the field of catalysis, electrochemistry, separation and biotechnology widely, leading to an increasing interest in both academic and industrial [17–19]. LDHs such as NiCo-LDH [10,20], CoMn-LDH [21,22], CoAl-LDH [23], NiAl-LDH [24,25], and NiMn-LDH [26,27] with many intrinsic features (high redox activity, adjustable chemical composition, large surface area with exposed, atoms intrinsic high stability and good anion exchange behavior) have been intensely explored as promising electrode materials for supercapacitors [28]. Nonetheless, the electrochemical properties and the practical value of the supercapacitors fabricated with LDHs are usually compromised by the intrinsic poor electron conductivity (10^{-13} to 10^{-17} S cm^{-1}) of LDHs [29]. Two strategies are

---

* Corresponding author.
** Corresponding author. College of Material Science and Engineering, Institute for Graphene Applied Technology Innovation, Collaborative Innovation Centre for Marine Biomass Fibers, Materials and Textiles of Shandong Province, Qingdao University, Qingdao 266071, Shandong, China.
E-mail addresses: cuiliang@lyu.edu.cn (L. Cui), jliu@qdu.edu.cn (J. Liu).

https://doi.org/10.1016/j.jallcom.2020.155321
0925-8388/

usually utilized to enhance the conductivity of LDHs. One strategy is generating composites or nanohybrids with enhanced conductivity via integrating LDHs nanostructures with other highly conductive materials [30]. Another effective strategy is synthesising trimetallic LDHs by doping or incorporation of another metal, through which the synergistic effect between the host metals and incorporated metals might change the electronic structure of the primitive bimetallic LDHs to the direction we desire [31].

Hence, combining the above two strategies, we report a simple method for fabricating binder-free $Cu_{2+1}O$@NiCoAl-layered double hydroxide ($Cu_{2+1}O$@NiCoAl-LDH) core-shell hybrid nanorod arrays on copper foam, in which the $Cu_{2+1}O$ nanorod arrays (NRAs) act as the core and the NiCoAl-LDH nanosheets act as the shell layer. The Cu foam with $Cu_{2+1}O$ NRAs is a promising substrate because the 3D porous copper foam and nanorod arrays could provide more channels to allow the electrolyte ions access the active LDH materials of electrodes more easily, which can decrease the agglomeration of NiCoAl-LDH nanosheets consequently [32,33]. The NiCoAl-LDH with ultrathin nanosheet morphology was grew on the surface of $Cu_{2+1}O$ NRAs directly, which can make the whole composites maintain good electrical conductivity. In addition, the CoNiAl-LDH nanosheets with high surface area can shorten the distance of ion transport and increase the utilization rate of the active materials [2]. The as-prepared $Cu_{2+1}O$@NiCoAl-LDH NRAs electrode presented an area capacitance of 7771 mF cm^{-2} (2932 F g^{-1}) at a current density of 2 mA cm^{-2}, outstanding rate capability (80.50% from 2 mA cm^{-2} to 20 mA cm^{-2}), and excellent cycling stability (maintained 94.27% of the initial capacitance after consecutive GCD test for 6000 cycles), which are significantly higher than those of $Cu(OH)_2$ and $Cu_{2+1}O$@NiCo-LDH electrodes.

Moreover, an HSC device assembled with the $Cu_{2+1}O$@NiCoAl-LDH and activated carbon (AC) as positive and negative electrodes respectively, exhibited excellent electrochemical performances. In detail, the $Cu_{2+1}O$@NiCoAl-LDH//AC HSC exhibited a maximum specific capacitance of 197.87 F g^{-1}, a high energy density of 61.83 Wh kg^{-1} at a power density of 749.93 W kg^{-1}. Furthermore, some LED indicators with different shape combination can be illuminated by HSC devices. Our work indicates that the $Cu_{2+1}O$@NiCoAl-LDH nanohybrids will be one of the most promising electrode materials for the application in high capacitive performance energy storage devices.

2. Experimental section

2.1. Materials

Aluminium nitrate nonahydrate ($Al(NO_3)_3 \cdot 9H_2O$, AR), nickel nitrate hexahydrate ($Ni(NO_3)_2 \cdot 6H_2O$, AR), urea (CH_4N_2O, AR), ammonium persulfate ($(NH_4)_2S_2O_8$, AR), cobalt nitrate hexahydrate ($Co(NO_3)_2 \cdot 6H_2O$, AR), sodium hydroxide (NaOH, AR), polyvinylidene fluoride (PVDF), potassium hydroxide (KOH, AR) and acetylene black were supplied by Sinopharm Chemical Reagent Co., Ltd. Hydrochloric acid (HCl, AR), acetone (AR) and ethanol (AR) were provided by Tianjin Fuyu Fine Chemical Co., Ltd. Activated carbon were supplied by Aladin GmbH Co., Ltd. The copper foam and nickel foam were purchased from Shanghai Zhongwei New Material Co., Ltd. The deionized (DI) water was produced by a Flom ultrapure water system.

2.2. Preparation of $Cu(OH)_2$ nanorod arrays precursor ($Cu(OH)_2$ NRAs) on copper foams

The copper foam (2.0×4.0 cm^2) was ultrasonically cleaned with HCl solution (37 wt%), acetone, ethanol and DI water in sequence for about 40 min to make sure that the surface oxide layer can be removed. Then the pretreated Cu foam was dried in a 60 °C vacuum for about 6 h. The $Cu(OH)_2$ NRAs were generated on the Cu foam (2.0×4.0 cm^2) by an in situ chemical oxidation with a solution consisted of NaOH (10.0 mL, 2.5 M) and $(NH_4)_2S_2O_8$ (10.0 mL, 0.125 M) for 10 min. After reaction, the Cu foam was swilled with ethanol and DI water for several times and then dried at 60 °C oven for about 6 h to get the $Cu(OH)_2$ NRAs. The calculated mass load of $Cu(OH)_2$ on the Cu foam is about 1.30 mg cm^{-2}.

2.3. Preparation of the $Cu_{2+1}O$@NiCoAl-LDH NRAs

The $Cu(OH)_2$ NRAs precursor (1.0×2.0 cm^2) was put into a 50 mL Telfon-lined stainless steel autoclave at 100 °C for 8 h, which have been previously charged with 20.0 mL freshly prepared aqueous solution consisted of urea (0.12 M), $Al(NO_3)_2 \cdot 6H_2O$ (4 mM), $Ni(NO_3)_2 \cdot 6H_2O$ (12 mM) and $Co(NO_3)_2 \cdot 6H_2O$ (4 mM). During the hydrothermal reaction, $Cu(OH)_2$ NRAs were dehydrated into $Cu_{2+1}O$ NRAs, and the NiCoAl-LDH nanosheets were generated on the surface of the $Cu_{2+1}O$ NRAs to form the core/shell structure. After the hydrothermal reaction, the $Cu(OH)_2$ NRAs precursor was swilled with absolute ethanol and DI water for several times and dried in a vacuum drying oven at 60 °C for 6 h to obtain hierarchical 3D branched $Cu_{2+1}O$@NiCoAl-LDH core/shell nanorod arrays on Cu foam. The calculated mass load of $Cu_{2+1}O$@NiCoAl-LDH NRAs branched on the Cu foam is about 2.65 mg cm^{-2}.

2.4. Synthesis of the $Cu_{2+1}O$@NiCo-LDH NRAs

The $Cu_{2+1}O$@NiCo-LDH NRAs were prepared by the same method as the preparation of $Cu_{2+1}O$@NiCoAl-LDH NRAs above, except that the 20.0 mL reaction solution was consisted of 0.14 M urea, 12 mM $Ni(NO_3)_2 \cdot 6H_2O$ and 12 mM $Co(NO_3)_2 \cdot 6H_2O$. The calculated mass load of $Cu_{2+1}O$@NiCo-LDH NRAs branched on the Cu foam is about 2.45 mg cm^{-2}.

2.5. Characterization

The morphologies of all samples were investigated by a scanning electron microscope (SEM, ZEISS Supra 55) at an accelerating potential of 10 kV and a transmission electron microscope (TEM, JEOL JEM-2010) with an accelerating voltage of 200 kV. The energy dispersive X-ray spectrometry (EDS) elemental mapping and spectrum analyses of the products were performed on a JEM-2010. X-ray diffraction (XRD, D/max-kA diffractometer) was applied to characterized the crystallographic structures of the samples. Specific surface areas were measured by a nitrogen adsorption-desorption system (BJ builder Kubo x1000) using the Brunauer-Emmet-Tell (BET) method. The compositions of the products were studied by X-ray photoelectron spectroscopy (XPS) on a PHI 5000C ESCA System.

2.6. Fabrication and electrochemical measurements of electrodes

All of the electrochemical tests were performed at room temperature with an electrochemical workstation (CHI 760E) (Shanghai Chenhua Instrument Factory, China). Cyclic voltammetry (CV), galvanostatic charge/discharge (GCD) and electrical impedance spectroscopy (EIS) measurements of the as-prepared positive electrode materials were performed by a three-electrode cell configuration in a 6.0 M KOH electrolyte. The tested samples (1.0×1.0 cm^2) was served as the working electrode directly, the platinum foil was served as the counter electrode, and the mercuric oxide electrode was served as the reference electrode. The active carbon electrode (negative electrode) was prepared by following procedure: First, the right amount of activated carbon (AC), acetylene black (conductive agent) and polyvinylidene fluoride (PVDF, binder) were weighed according to the mass ratio of 8:1:1, and mixed with ethanol to produce a slurry. Then the above slurry was painted onto the surface of nickel foam substrate (1.0×1.0 cm^2) uniformly and dried at 60 °C vacuum oven for 8 h to obtain the AC electrode in the end. The area capacitance (C_A) and specific capacitance (C_S) can be obtained based on equations (1) and (2) according to the GCD curves [32].

$$C_A = \frac{I\Delta t}{s\Delta U} \tag{1}$$

$$C_S = \frac{I\Delta t}{m\Delta U} \tag{2}$$

where I (A) is the discharge current, ΔU (V) is the potential window, Δt (s) is the discharge time, C_A (F·cm^{-2}) is the area capacitance, s (cm^2) is the area of active materials, C_S (F·g^{-1}) is the specific capacitance, and m (g) is the mass of active materials.

2.7. Fabrication and electrochemical measurements of hybrid supercapacitor (HSC)

As for two-electrode tests, the $Cu_{2+1}O$@NiCoAl-LDH electrode (1.0×1.0 cm^2) was the positive electrode and the AC electrode was the negative one with a potassium hydroxide (KOH) aqueous solution at a concentration of 6 M as electrolyte. The best electrochemical performance can achieve only when the charge balance between the two electrodes follow the relationship ($q+ = q-$, $q = mC\Delta U$). The ideal mass ratio of $Cu_{2+1}O$@NiCoAl-LDH and AC electrodes in an HSC (m^+/m^-) can be obtained by equation (3) [34].

$$m^+ / m^- = C^-\Delta U^- / C^+\Delta U^+ \tag{3}$$

where C^+ (F g^{-1}) and C^- (F g^{-1}) are the specific capacitance of $Cu_{2+1}O$@NiCoAl-LDH and AC electrodes, respectively. ΔU^+ (V) and ΔU^- (V) are the potential range of one scanning segment of $Cu_{2+1}O$@NiCoAl-LDH and AC electrodes, respectively. Furthermore, the energy density (E, Wh kg^{-1}) and power density (P, W kg^{-1}) of the HSC device can be obtained according to equation (4) and equation (5) as below [35]:

$$E = \frac{1}{2} C_s \Delta U^2 \tag{4}$$

$$P = E / \Delta t \tag{5}$$

where the C_s of the HSC device can be obtained by equation (2), but the m (g) is the gross mass of active materials for the two electrodes.

The all solid-state HSC device was fabricated by applying the $Cu_{2+1}O$@NiCoAl-LDH electrode and AC electrode as positive and negative electrode, respectively. The electrolyte is PVA/KOH gel, which was prepared by the following detailed procedure: A mixture consisted of 3.0 g PVA and 20.0 mL DI water was heated at 90 °C for about 1 h under vigorous stirring to make the PVA dissolve completely. When the solution temperature drops to 60 °C, 10.0 mL of 1.0 M KOH aqueous solution was dripped into the solution while vigorous stirring and keep stirring for half an hour. Cool the solution to room temperature to remove the bubbles to get the transparent PVA/KOH gel electrolyte. The surface of $Cu_{2+1}O$@NiCoAl-LDH (2.0×2.0 cm^2) and AC electrodes were covered with above gel electrolyte to assembled together to obtain an HSC device. Finally, the assembled $Cu_{2+1}O$@NiCoAl-LDH//AC HSC device was dried at a 40 °C vacuum oven for about 12 h to remove the moisture to obtain an all solid-state HSC device.

3. Results and discussion

The preparation process of the $Cu_{2+1}O$@NiCo-LDH and $Cu_{2+1}O$@NiCoAl-LDH materials is schematically illustrated in Fig. 1. As our previous work reported, the $Cu(OH)_2$ NRAs could be grown vertically on Cu foam by an easy in situ chemical oxidation reaction [33]. After a one-step hydrothermal treatment in different reaction solution, the $Cu(OH)_2$ NRAs were dehydrated into $Cu_{2+1}O$ NRAs and a layer of NiCo-LDH nanothorns or NiCoAl-LDH nanosheets were generated on the surface of the nanorods concurrently. In the process of hydrothermal synthesis, the NH_3 released from the urea will increase the concentration of OH^-, which will react with Ni^{2+}, Co^{2+} and Al^{3+} in the solution to form nanosized LDH particles on the surface of $Cu_{2+1}O$ NRAs backbone. These $Cu_{2+1}O$@NiCo-LDH and $Cu_{2+1}O$@NiCoAl-LDH NRAs directly grown on Cu foam substrate to form a binder-free structure electrode to enhance the conductivity dramatically as a result of the reduced contact resistance between the substrate and the active materials.

Fig. 2a–f shows the SEM images at different magnifications of the as-obtained $Cu(OH)_2$, $Cu_{2+1}O$@NiCo-LDH and $Cu_{2+1}O$@NiCoAl-LDH NRAs supported on the 3D copper foam. As indicated in Fig. 2a and d, the surface of the $Cu(OH)_2$ NRAs is smooth and the average dimeter of nanorods is about 200 nm. Fig. 2b and e show that countless NiCo-LDH nanothorns are generated on the surface of $Cu_{2+1}O$ nanorods evenly after the hydrothermal treatment. While the morphology of the NiCoAl-LDH grown on the surface of $Cu_{2+1}O$ nanorods is nanosheet upon the addition of Al^{3+}. According to the SEM images of the $Cu_{2+1}O$@NiCoAl-LDH (Fig. 2c and f), it is obvious to observe that the NiCo-LDH nanothorns can transform into NiCoAl-LDH nanosheets by incorporating the metal Al element into NiCo-LDH.

TEM, HRTEM and EDS elemental mapping analyses of the samples were also carried out to analyze their detailed structure. Fig. 3a–c show the different morphologies of $Cu(OH)_2$, $Cu_{2+1}O$@NiCo-LDH and $Cu_{2+1}O$@NiCoAl-LDH, which are in accord with the SEM images. From the HRTEM image of $Cu_{2+1}O$@NiCoAl-LDH in Fig. 3d, it is obviously seen that the diameter of the $Cu_{2+1}O$ nanorod is smaller than that of pristine $Cu(OH)_2$ nanorod, but the structure of nanorod keeps well. An interplanar spacing of 0.26 nm corresponding to the characteristic (012) plane of NiCoAl-LDH nanosheets is also found with the $Cu_{2+1}O$@NiCoAl-LDH, further confirming the formation of the crystallized LDH phase, as shown in Fig. 3e [28]. Moreover, the EDS spectrum shown in Fig. 3f manifests that the $Cu_{2+1}O$@NiCoAl-LDH is composed of Cu, Co, Ni, Al and O elements, and the corresponding ratios of these elements are shown in the inset of Fig. 3f. From the EDS elemental mapping images shown in Fig. 3g, it can be seen that Cu is mainly distributed in the backbone region, while Co, Ni, Al and O are evenly throughout the trunk and branch regions, suggesting that the $Cu_{2+1}O$ nanorod have been successfully covered with the NiCoAl-LDH nanosheets.

The XRD patterns of $Cu_{2+1}O$@NiCoAl-LDH and $Cu_{2+1}O$@NiCo-LDH are exhibited in Fig. 4a. Meanwhile, the XRD pattern of precursor $Cu(OH)_2$ is presented in Fig. S1. Three strong diffraction peaks at 2θ of 43.3°, 50.4° and 74.1° can be observed in all the three patterns, which are corresponding to the (111), (200) and (220) facets respectively of metallic Cu (JCPDS no. 04–0836). As shown in Fig. S1a and Fig. 4a, the diffraction peaks at 2θ of 16.6°, 23.8°, 33.8°, 35.7°, 39.8° and 53.2° are resulted from $Cu(OH)_2$ (JCPDS no. 13–0420), while the peaks at 2θ of 29.5°, 36.4°, 42.3°, 61.3° and 77.3° are corresponding to $Cu_{2+1}O$ (JCPDS no. 05–0667), indicating that the $Cu(OH)_2$ was transformed to $Cu_{2+1}O$ successfully. Two patterns all show diffraction peaks at 2θ of 11.7°, 23.2°, 34.8° and

Fig. 1. Schematic illustration for the preparation of the Cu$_{2+1}$O@NiCo-LDH and Cu$_{2+1}$O@NiCoAl-LDH materials.

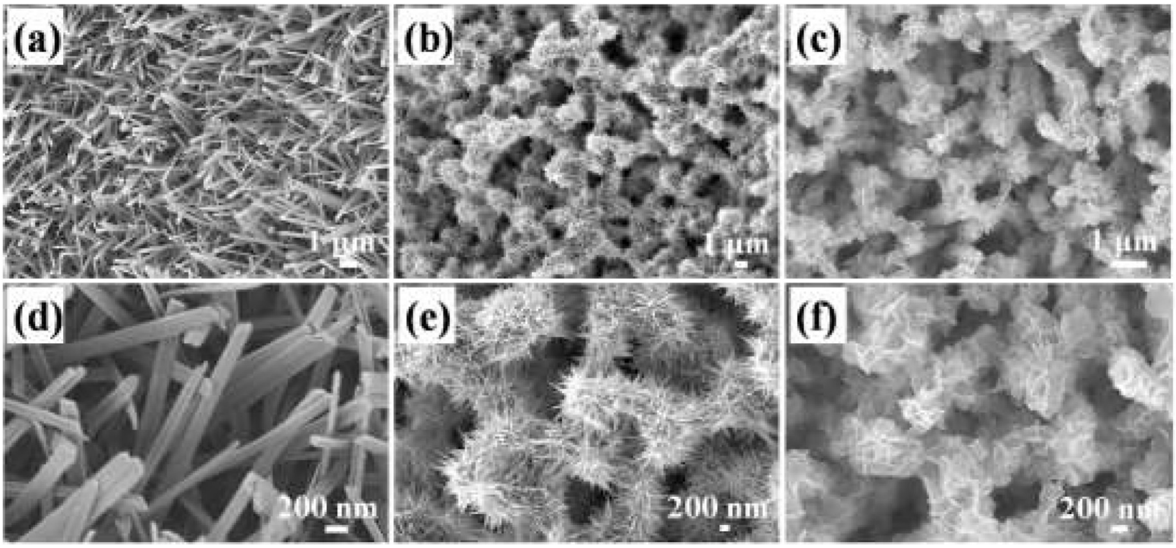

Fig. 2. SEM images of (a, d) Cu(OH)$_2$, (b, e) Cu$_{2+1}$O@NiCo-LDH and (c, f) Cu$_{2+1}$O@NiCoAl-LDH obtained at different magnifications.

39.5°, which correspond to (003), (006), (012) and (015) crystal faces of LDH hydrotalcite structure reported in previous literature, respectively [1,28,36–39].

XPS results of the Cu$_{2+1}$O@NiCoAl-LDH are shown in Fig. 4c–f and Fig. S2, which can be utilized to study the valence state of the elements. The complete spectrum presented in Fig. S2a manifests the existence of Cu, Al, Ni, Co and O elements, which is identify with the EDS results. From the high resolution spectrum for Ni 2p displayed in Fig. 4c, it can be observed that the peaks at 856.3 and 873.4 eV are ascribed to the characteristic 2p$_{3/2}$ and 2p$_{1/2}$ peaks for Ni^{2+}, and the peaks at 857.9 and 875.8 eV can be assigned to the featured 2p$_{3/2}$ and 2p$_{1/2}$ peaks of Ni^{3+}, respectively [11,31]. In the Co 2p spectrum (Fig. 3d), the peaks at 783.8 and 800.1 eV should correspond to Co 2p$_{3/2}$ and Co 2p$_{1/2}$, which are the characteristic peaks of Co^{2+} in Co(OH)$_2$. The peaks at 781.8 and 797.7 eV correspond to the Co 2p$_{3/2}$ and Co 2p$_{1/2}$ of Co^{3+}, separately [31,40]. As exhibited in Fig. 4e, the binding energies of Cu 2p$_{3/2}$ (934.8 eV) and Cu 2p$_{1/2}$ (954.9 eV) can be ascribed to the paramagnetic chemical state of Cu^{2+} [41], while the two peaks at 952.1 and 932.2 eV should correspond to the Cu 2p$_{1/2}$ and Cu 2p$_{3/2}$ peaks of Cu^{+}, respectively, demonstrating the existence of Cu$_{2+1}$O in the prepared Cu$_{2+1}$O@NiCoAl-LDH material [42]. The Al 2p spectrum in Fig. 4f could be separated into two peaks centered at 68.5 and 74.1 eV, corresponding to the featured 2p$_{3/2}$ and 2p$_{1/2}$ peaks of Al^{3+} [43].

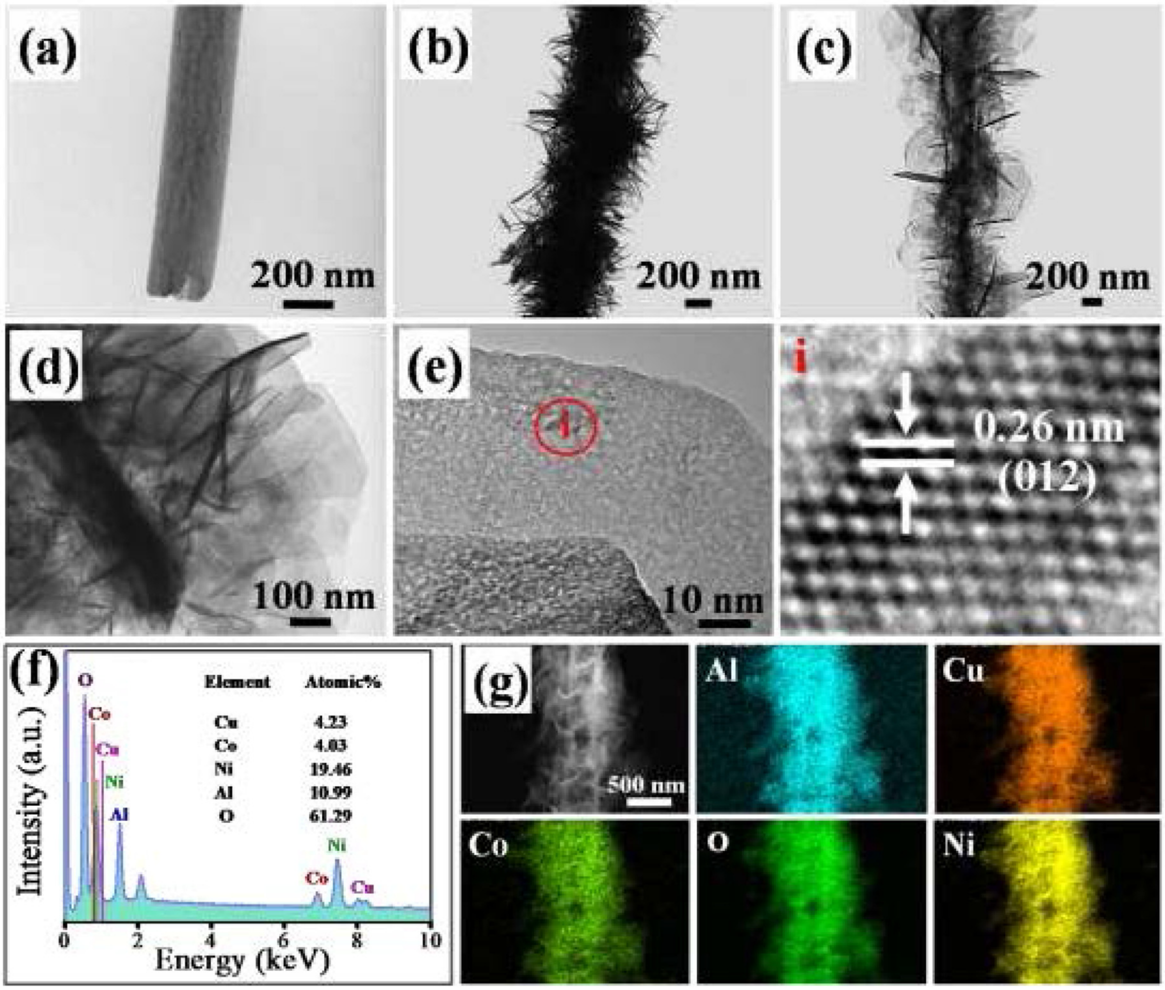

Fig. 3. TEM images of (a) $Cu(OH)_2$ (b) $Cu_{2+1}O$@NiCo-LDH, and (c, d) $Cu_{2+1}O$@NiCoAl-LDH. (e) HRTEM, (f) EDS spectrum, and (g) EDS elemental mapping images of $Cu_{2+1}O$@NiCoAl-LDH.

The O 1s spectrum (Fig. S2b) can be separated into three peaks, which should result from the oxygen existing in the form of H_2O, $M - OH$ and $M - O$ (M represents metal element) [44,45]. All of above results indicate that the NiCoAl-LDH nanosheets are successfully generated on the surface of the $Cu_{2+1}O$ nanorods to form a core-shell hierarchical architecture.

The electrochemical properties of $Cu(OH)_2$, $Cu_{2+1}O$@NiCo-LDH and $Cu_{2+1}O$@NiCoAl-LDH electrodes were characterized in a three-electrode cell under a voltage range of 0–0.5 V. Fig. 5a shows the CV curve comparison diagram of the three electrodes at the same scan rate (50 mV s^{-1}). Apparently, Compared with $Cu(OH)_2$ and $Cu_{2+1}O$@NiCo-LDH electrodes, the CV integrated area of the $Cu_{2+1}O$@NiCoAl-LDH electrode is the largest, indicating that the electrochemical activity is greatly enhanced as a result of the synergistic effect of multi metals and the high specific surface area resulting from the unique core/shell structure. Fig. 5b is a comparison of GCD curves of as-prepared three electrodes at current density of 2 mA cm^{-2}. Obviously, the discharge time of the $Cu_{2+1}O$@NiCoAl-LDH electrode is much longer than that of the other two electrodes, which means that the specific capacitance of the $Cu_{2+1}O$@NiCoAl-LDH electrode is the highest. In detail, the area capacitances at a current density of 2 mA cm^{-2} of $Cu(OH)_2$, $Cu_{2+1}O$@NiCo-LDH and $Cu_{2+1}O$@NiCoAl-LDH electrodes are 338, 4376 and 7771 mF cm^{-2} (2932 F g^{-1}), respectively. In addition, we compare the specific capacitance and cycling properties of the as-prepared $Cu_{2+1}O$@NiCoAl-LDH electrode with the recently reported LDH materials and displayed the results in Table S1. This indicates that the $Cu_{2+1}O$@NiCoAl-LDH owns outstanding capacitive properties and can be a good material choice for preparing supercapacitor electrodes.

A battery of systematic electrochemical testing (CV, GCD, EIS and cycling performance) were performed to further study the electrochemical performance of the $Cu_{2+1}O$@NiCoAl-LDH electrode ulteriorly. As exhibited in Fig. 5c, the shape of CV curves maintains well with the increasing scan rate from 5 to 50 mV s^{-1}, indicating that the unique core-shell architecture of $Cu_{2+1}O$@NiCoAl-LDH electrode is benefit to rapid redox reactions or high cycling rates. The redox reactions that occur in the process of CV test can be explained as below [46]:

$$Co(OH)_2 + OH^- \Leftrightarrow CoOOH + H_2O + e^- \tag{6}$$

$$CoOOH + OH^- \Leftrightarrow CoO_2 + H_2O + e^- \tag{7}$$

$$Ni(OH)_2 + OH^- \Leftrightarrow NiOOH + H_2O + e^- \tag{8}$$

For comparison, the CV curves of the $Cu(OH)_2$ and $Cu_{2+1}O$@NiCo-LDH electrodes at different scan rates (5–50 mV s^{-1}) are also measured. As presented in Fig. S3a and d, the peak current

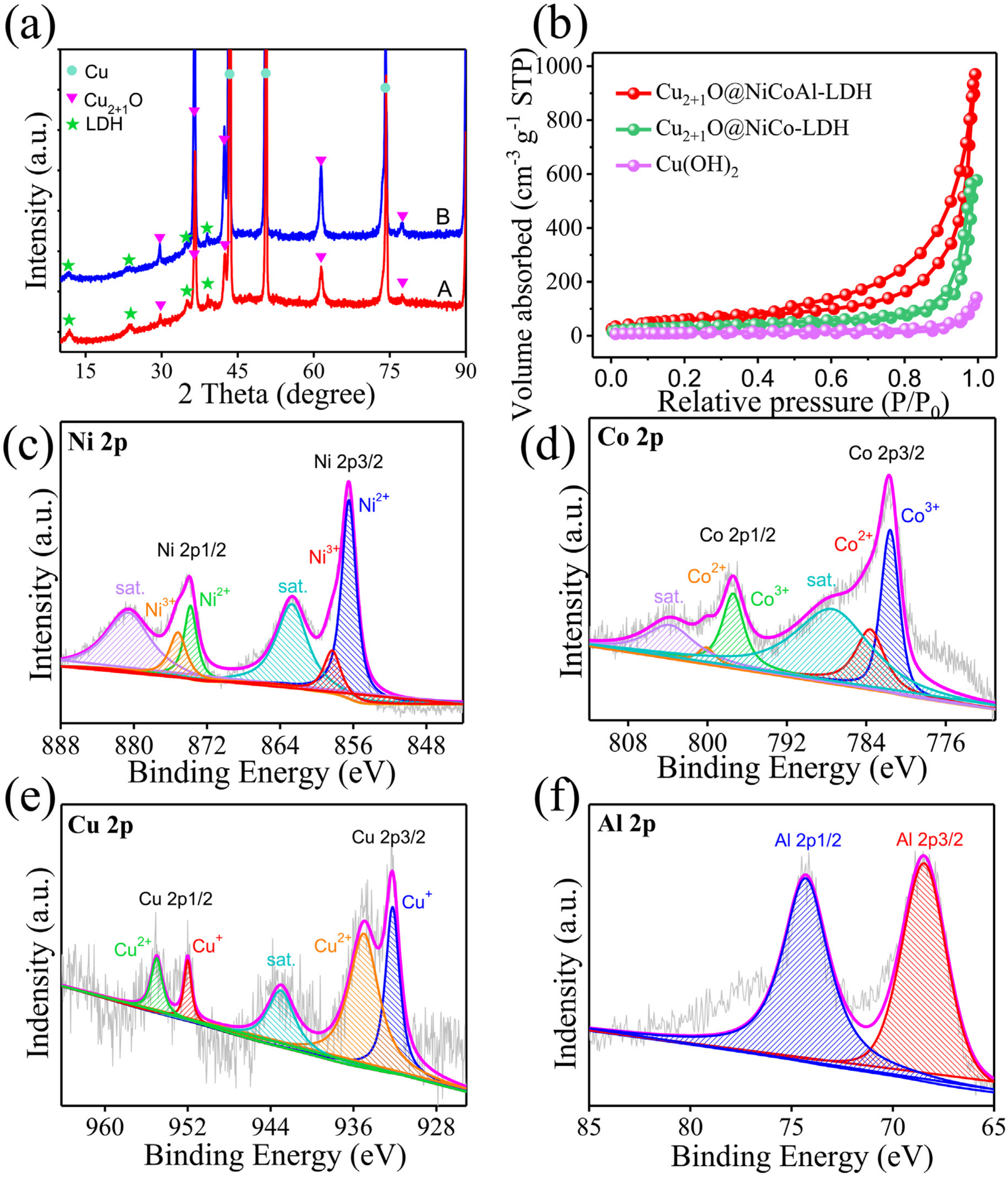

Fig. 4. (a) The XRD patterns of the (A) $Cu_{2+1}O$@NiCoAl-LDH and (B) $Cu_{2+1}O$@NiCo-LDH. (b) Nitrogen adsorption-desorption isotherms of $Cu_{2+1}O$@NiCoAl-LDH, $Cu_{2+1}O$@NiCo-LDH and $Cu(OH)_2$. High-resolution XPS spectra for (c) Ni 2p, (d) Co 2p, (e) Cu 2p and (f) Al 2p of $Cu_{2+1}O$@NiCoAl-LDH.

and integrated area of CV curves for these samples are all smaller than that of the $Cu_{2+1}O$@NiCoAl-LDH electrode.

All GCD curves of $Cu_{2+1}O$@NiCoAl-LDH electrode (Fig. 5d) display symmetric charge-discharge characteristics and the discharge times decreases with the increase of current density, indicating that the $Cu_{2+1}O$@NiCoAl-LDH electrode has outstanding reversibility in the charge-discharge process. For comparison, GCD curves of $Cu(OH)_2$ and $Cu_{2+1}O$@NiCo-LDH electrodes obtained from various current densities are presented in Fig. S3b and e and the relationship between specific capacitance of these electrode materials and current density are presented in Fig. 5e. As the current density increases from 2 to 20 mA cm^{-2}, the capacitance value of the $Cu_{2+1}O$@NiCoAl-LDH electrode remains 80.50% of the initial value, demonstrating a remarkable rate capability, which is much greater than that of $Cu(OH)_2$ (46.15%) and $Cu_{2+1}O$@NiCo-LDH (77.01%) electrodes. Such improvements of capacitive performance should be likely due to the increase in surface area, as confirmed by BET results (Fig. 4b). The surface area of $Cu(OH)_2$, $Cu_{2+1}O$@NiCo-LDH and $Cu_{2+1}O$@NiCoAl-LDH is 31.63 m^2/g, 105.03 m^2/g and 201.28 m^2/g, respectively.

The electrochemical conductivities of $Cu(OH)_2$, $Cu_{2+1}O$@NiCo-LDH and $Cu_{2+1}O$@NiCoAl-LDH electrodes were further studied by

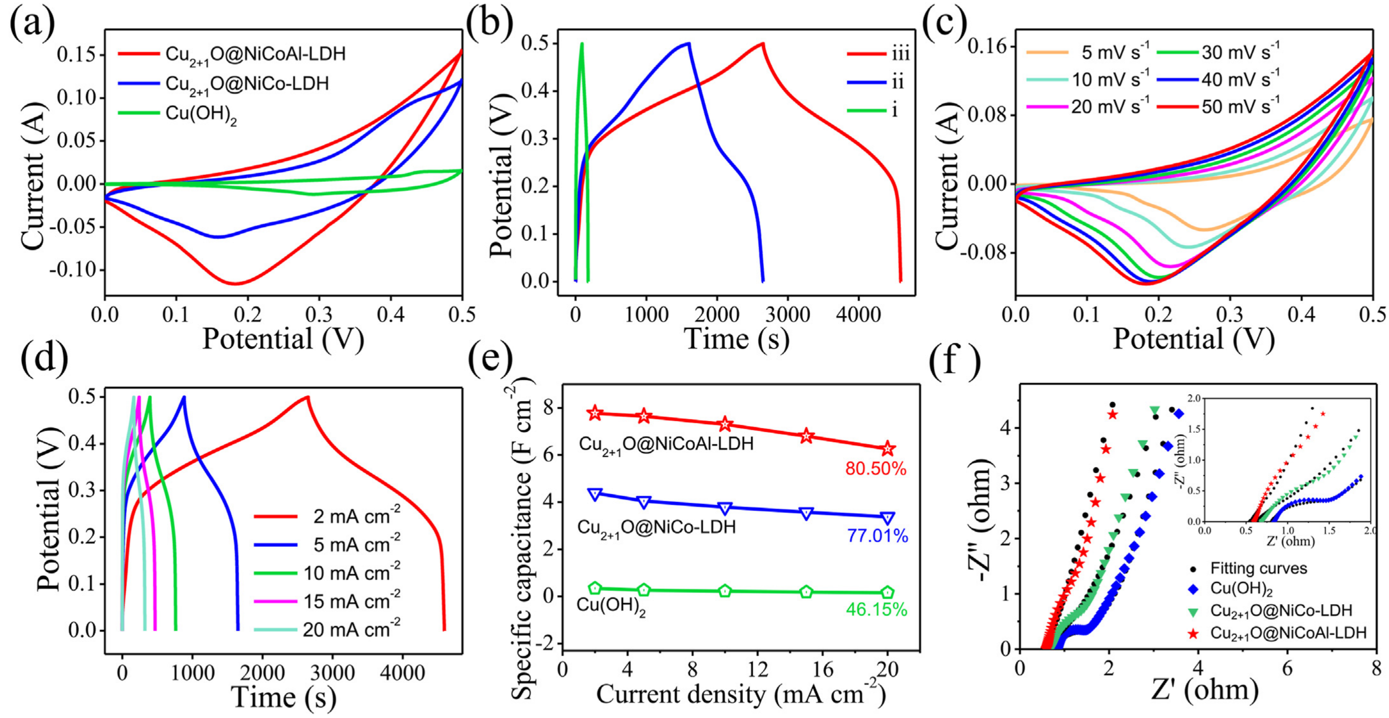

Fig. 5. (a) CV curves of $Cu(OH)_2$, $Cu_{2+1}O$@NiCo-LDH and $Cu_{2+1}O$@NiCoAl-LDH electrodes at a scan rate of 50 mV s^{-1}. (b) GCD curves of (i) $Cu(OH)_2$, (ii) $Cu_{2+1}O$@NiCo-LDH and (iii) $Cu_{2+1}O$@NiCoAl-LDH electrodes at a current density of 2 mA cm^{-2}. (c) CV curves of the $Cu_{2+1}O$@NiCoAl-LDH electrode at various scan rates. (d) GCD curves of the $Cu_{2+1}O$@NiCoAl-LDH electrode at different current densities. (e) Capacitance retention of $Cu(OH)_2$, $Cu_{2+1}O$@NiCo-LDH and $Cu_{2+1}O$@NiCoAl-LDH electrodes at different current densities. (f) Nyquist plots and fitting curves of $Cu(OH)_2$, $Cu_{2+1}O$@NiCo-LDH and $Cu_{2+1}O$@NiCoAl-LDH electrodes. The insets show the plots in high-frequency range.

EIS test, and the Nyquist plots and fitting curves of these three electrodes are displayed in Fig. 5f. The slope of the straight line in low-frequency areas represents the diffusion resistance (R_W) of ions, which describes the diffusion process of the ions in the redox reaction kinetics [47]. From Fig. 5f, it can be clearly seen that the R_W of the $Cu_{2+1}O$@NiCoAl-LDH electrode is significantly smaller than that of $Cu(OH)_2$ and $Cu_{2+1}O$@NiCo-LDH electrodes. In the high frequency region, the diameter of the semicircle indicates the charge transfer resistance (R_{ct}) of the electrode, while the intercept of the x-axis represents the equivalent series resistance (R_s) of the electrode, which includes the total resistance of the active material, the current collector and the electrolyte [48,49]. According to the inset of Fig. 5f, a smallest intercept of the x-axis of $Cu_{2+1}O$@NiCoAl-LDH electrode among all electrode materials studied can be observed, demonstrating that the $Cu_{2+1}O$@NiCoAl-LDH electrode has the lowest R_s. Specifically, the R_s of $Cu(OH)_2$, $Cu_{2+1}O$@NiCo-LDH and $Cu_{2+1}O$@NiCoAl-LDH electrodes are 0.87 Ω, 0.67 Ω and 0.58 Ω, respectively, which can be obtained by the fitting curves of these three electrodes. Similarly, the diameter of the semicircle for the $Cu_{2+1}O$@NiCoAl-LDH electrode in low-frequency areas is the smallest, suggesting the lowest R_{ct}. According to the results above, it can be concluded that the $Cu_{2+1}O$@NiCoAl-LDH with good electronic conductivity and charge-transfer capability could be a potential electrode material for supercapacitors.

The cycling performance and coulombic efficiency of $Cu_{2+1}O$@NiCoAl-LDH electrode was studied by a three-electrode cell at a high current density of 20 mA cm^{-2} for 6000 consecutive GCD cycles, and the results are exhibited in Fig. 6a. The $Cu_{2+1}O$@NiCoAl-LDH electrode shows high area capacitance and can maintain well during the initial cycles, but the capacitance decreases slowly with the increasing cycles and still retains about 94.27% of its original capacitance after 6000 successive GCD cycles, indicating the good stability. Meanwhile, the coulombic efficiency can also retain 98.73%. In addition, the SEM image and XRD pattern of the $Cu_{2+1}O$@NiCoAl-LDH electrode after cycling test are shown in Fig. S4 to evaluate the stability of the electrode material. From Fig. S4a, we can see that the framework of $Cu_{2+1}O$@NiCoAl-LDH nanorods maintained well, but the NiCoAl-LDH nanosheets deformed slightly, indicating the good structural stability and remarkable cycling stability of the electrode material. The XRD pattern of the $Cu_{2+1}O$@NiCoAl-LDH electrode after the cyclic test was basically consistent with that before the test, indicating the good stability of the electrode material.

The desirable advantages of the $Cu_{2+1}O$@NiCoAl-LDH electrode can be illustrated as follows on the basis of the schematic diagram shown in Fig. 6b. First, Cu foam is a promising substrate as a result of its three dimensional open-porous structure, excellent conductivity, high specific surface area and low cost [50]. Second, the $Cu_{2+1}O$ NRAs transformed from the $Cu(OH)_2$ NRAs growing directly on the surface of Cu foam maintains a good structure of the nanorod arrays, which can serve as a skeleton for the generation of NiCoAl-LDH nanosheets to maintain good mechanical connection and electronic transmission with the current collector [33]. Third, the ultra-thin NiCoAl-LDH nanosheets generated on the surface of the $Cu_{2+1}O$ nanorod arrays directly to develop a core/shell structure, which can effectively avoid agglomeration to increase the specific surface area [50]. Meanwhile, the grain boundary connectivity of ultra-thin NiCoAl-LDH nanosheet structures is usually remarkable, which can make the contact between nanosheets and electrolyte more close, thus accelerate the transfer of interface charge and improve the electrochemical reactions [51,52]. Finally, Ni and Co elements provide the psedocapacitance through the Faradaic reactions, while Al element can can make the LDH structure more stable, thus improving the cyclic stability of the electrode [11]. The synergistic action among the three metal elements could improve the electrical conductivity and reduce the charge transfer

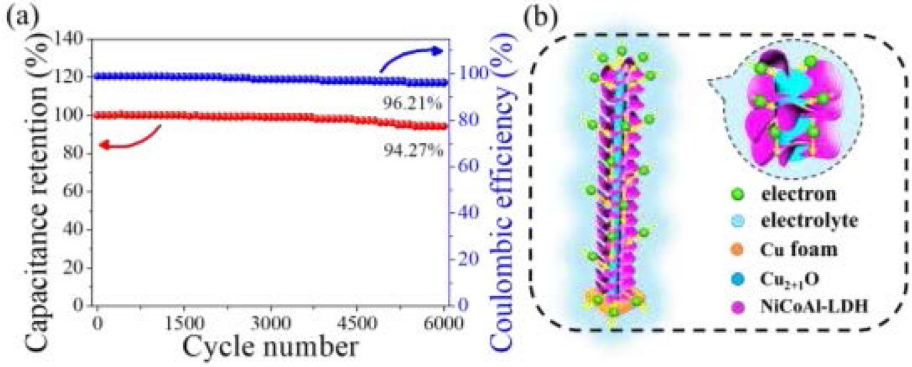

Fig. 6. (a) Cycling performance and Coulombic efficiency of $Cu_{2+1}O$@NiCoAl-LDH electrode at a current density of 20 mA cm^{-2}. (b) Schematic diagram interpreting the merits of the $Cu_{2+1}O$@NiCoAl-LDH electrode.

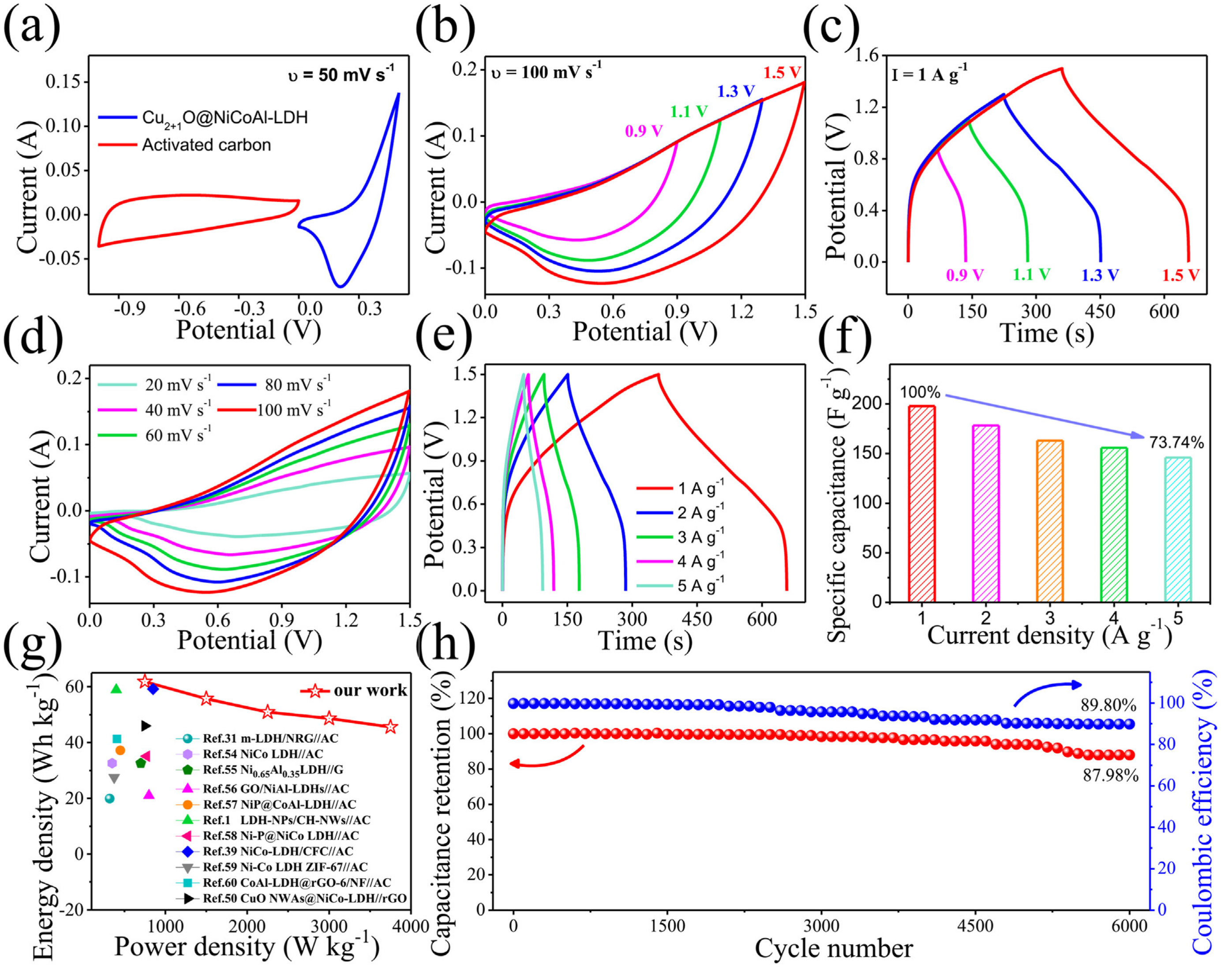

Fig. 7. (a) CV curves of $Cu_{2+1}O$@NiCoAl-LDH and AC electrodes obtained at a scan rate of 50 mV s^{-1} in a three-electrode system. (b) CV curves of the HSC in different potential ranges at the scan rate of 100 mV s^{-1}. (c) GCD curves of the HSC in different potential ranges at a current density of 1 A g^{-1}. (d) CV curves of the HSC at various scan rates. (e) GCD curves of the HSC at various current densities. (f) Capacitance retentions of the HSC at different current densities. (g) Ragone plots of our HSC and recently reported HSCs. (h) Cycling performance and Coulombic efficiency of the HSC measured at 5 A g^{-1} for 6000 cycles.

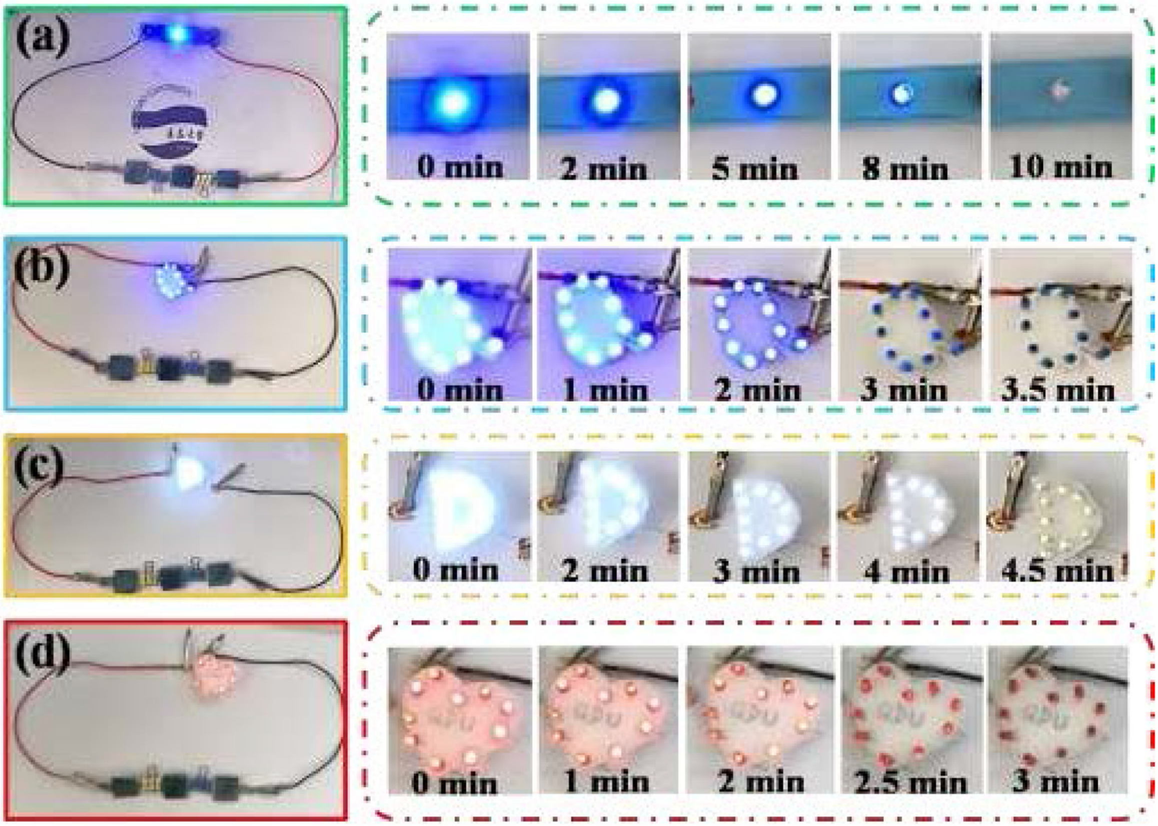

Fig. 8. Photographic images of the solid-state hybrid supercapacitors for lightning (a) the blue LED bulb, (b) the letter "Q" composed of 10 blue LED indicators in parallel, (c) the letter "D" composed of 10 yellow LED indicators in parallel and (d) a heart-shaped combination of ten red LED indicators connected in parallel. (For interpretation of the references to color in this figure legend, the reader is referred to the Web version of this article.)

resistance, leading to enhanced electrochemical performance of the $Cu_{2+1}O$@NiCoAl-LDH electrode [53].

In order to illustrate the practical value of the $Cu_{2+1}O$@NiCoAl-LDH electrode, an HSC ($Cu_{2+1}O$@NiCoAl-LDH//AC) was fabricated using $Cu_{2+1}O$@NiCoAl-LDH NRAs as the positive electrode, the AC coated Ni foam as the negative one and 6 M KOH as electrolyte. Electrochemical tests were also performed for the negative electrode (AC), the results of which are presented in Fig. S5, including CV, GCD, and rate capacity curves. The comparative CV curves of $Cu_{2+1}O$@NiCoAl-LDH and AC electrodes at a scan rate of 50 mV s^{-1} are shown in Fig. 7a, in which the voltage windows of the AC and $Cu_{2+1}O$@NiCoAl-LDH electrodes are −1.0 - 0 V and 0–0.5 V, respectively. Therefore, the obtained $Cu_{2+1}O$@NiCoAl-LDH//AC HSC can work in a broad voltage windows of 0–1.5 V. As seen in Fig. 7b, the CV curves of the $Cu_{2+1}O$@NiCoAl-LDH//AC HSC obtained at 100 mV s^{-1} in different potential windows indicating that the potential window of the $Cu_{2+1}O$@NiCoAl-LDH//AC HSC can be extended to 1.5 V and the shape of CV curves do not change obviously with the increasing working voltage window. Fig. 7c exhibits the GCD curves of the $Cu_{2+1}O$@NiCoAl-LDH//AC HSC under different voltage windows, which are measured under the current density of 1 A g^{-1}. Obviously, all the GCD curves are basically symmetric and the shape does not deform significantly as the voltage window expands, reflecting the ideal capacitive characteristics. The CV curves of the $Cu_{2+1}O$@NiCoAl-LDH//AC HSC at different scan rates in a voltage range of 0–1.5 V are shown in Fig. 7d. Deserved to be mentioned, the shape of the CV curves kept well with the increasing sweep rate from 20 to 100 mV s^{-1}, demonstrating the excellent rate capability of the $Cu_{2+1}O$@NiCoAl-LDH//AC HSC. The shape of the GCD curves of the $Cu_{2+1}O$@NiCoAl-LDH//AC HSC at different current densities are non-linear and nearly symmetrical, suggesting a battery-type capacitor behavior and high columbic efficiency (Fig. 7e). Moreover, the capacitance retention of the HSC at different current densities was exhibited in Fig. 7f. It can be seen that when the current density is 1 A g^{-1}, the specific capacitance can be as high as 197.87 F g^{-1}, while when the current density is increased to 5 A g^{-1}, the specific capacitance can still retain 73.74%.

To evaluate the entire HSC device, the energy and power density were investigated and the Ragone plots of the $Cu_{2+1}O$@NiCoAl-LDH//AC HSC were shown in Fig. 7g. The HSC exhibits an excellent energy density of 61.83 Wh kg^{-1} at a power density of 749.93 W kg^{-1}. The HSC still retains a high energy density of 45.59 Wh kg^{-1} even at a higher power density of 3749.67 W kg^{-1}, which are superior to most of those previously reported on LDH-based HSCs as shown in Fig. 7g [1,31,39,50,54–60]. The cycling behavior and columbic efficiency of the $Cu_{2+1}O$@NiCoAl-LDH HSC were measured at 5 A g^{-1} for 6000 cycles. Fig. 7h showing that the HSC retained 87.98% of its initial specific capacitance and 89.80% of its initial coulombic efficiency, indicating the remarkable cyclic stability and electrochemical reversibility.

In addition, a few LED indicators assembled with different shape combinations were lit up to demonstrate the practical utility of the HSC device. As shown in Fig. 8a, a blue LED indicator can be illuminated by three all-solid state HSCs connected in series for about 10 min. Fig. 8b–d show that when ten LED indicators with blue, yellow and red colors are connected in parallel into different shape combinations of "Q", "D" and "heart", they can be illuminated by three all-solid state HSCs connected in series for about 3.5, 4.5, and 3 min, respectively.

4. Conclusion

The $Cu_{2+1}O$@NiCoAl-LDH core-shell nanorod arrays have been designed and fabricated on copper foams successfully. The well-aligned $Cu_{2+1}O$ nanorod arrays are transformed from the $Cu(OH)_2$ nanorod arrays growing directly on the Cu foams, retaining a good three-dimensional skeleton structure that is conducive to the growth of NiCoAl-LDH nanosheets, electron transfer and ion diffusion. The specific capacitance (2932 F g^{-1} at 0.75 A g^{-1}) and cyclic stability (94.27% of the initial capacitance maintained after GCD test for 6000 cycles) of the $Cu_{2+1}O$@NiCoAl-LDH electrode obtained by electrochemical test are much better than those of $Cu(OH)_2$ and $Cu_{2+1}O$@NiCo-LDH electrodes. In addition, the HSC device assembled by $Cu_{2+1}O$@NiCoAl-LDH positive electrode and AC negative electrode can reach the high energy density of 61.83 Wh kg^{-1} at the power density of 749.93 W kg^{-1}. Furthermore, when LED indicators are connected into different shape combinations they can be illuminated by the assembled HSC devices, demonstrating the practical value of the HSC device. Our work indicates that structural design and composition optimization can improve the capacitance performance of electrode materials effectively.

Declaration of competing interest

The authors declare that they have no known competing financial interests or personal relationships that could have appeared to influence the work reported in this paper.

CRediT authorship contribution statement

Ying Liu: Conceptualization, Methodology, Data curation, Writing - original draft, Writing - review & editing. **Xueying Cao:** Writing - review & editing. **Yuxue Zhong:** Investigation. **Liang Cui:** Funding acquisition. **Di Wei:** Writing - review & editing. **Rongkun Zheng:** Writing - review & editing. **Jingquan Liu:** Writing - review & editing, Resources, Project administration, Funding acquisition.

Acknowledgments

The authors are thankful to funds from Double-Hundred Foreign Experts Program of Shandong, Natural Science Foundation of China (21805124), and Natural Science Foundation of Shandong Province (ZR2018BEM020).

Appendix A. Supplementary data

Supplementary data related to this article can be found at https://doi.org/10.1016/j.jallcom.2020.155321.

References

[1] J. Yang, C. Yu, X. Fan, J. Qiu, 3D architecture materials made of NiCoAl-LDH nanoplates coupled with NiCo-carbonate hydroxide nanowires grown on flexible graphite paper for asymmetric supercapacitors, Adv. Energy Mater. 4 (2014) 1400761.

[2] P. Huang, C. Cao, Y. Sun, S. Yang, F. Wei, W. Song, One-pot synthesis of sandwich-like reduced graphene oxide@CoNiAl layered double hydroxide with excellent pseudocapacitive properties, J. Mater. Chem. A. 3 (2015) 10858–10863.

[3] X. Cao, X. Wang, L. Cui, D. Jiang, Y. Zheng, J. Liu, Strongly coupled nickel boride/graphene hybrid as a novel electrode material for supercapacitors, Chem. Eng. J. 327 (2017) 1085–1092.

[4] R. Wang, Y. Lu, L. Zhou, Y. Han, J. Ye, W. Xu, X. Lu, Oxygen-deficient tungsten oxide nanorods with high crystallinity: promising stable anode for asymmetric supercapacitors, Electrochim. Acta 283 (2018) 639–645.

[5] Q. Zhang, W. Xu, J. Sun, Z. Pan, J. Zhao, X. Wang, et al., Constructing ultrahigh#capacity Zinc#Nickel#Cobalt Oxide@Ni$(OH)_2$ core-shell nanowire arrays for high-performance coaxial fiber-shaped asymmetric supercapacitors, Nano Lett. 7 (2017).

[6] Q. Zhang, J. Sun, Z. Pan, J. Zhang, J. Zhao, X. Wang, C. Zhang, Y. Yao, W. Lu, Q. Li, Y. Zhang, Z. Zhang, Stretchable fiber-shaped asymmetric supercapacitors with ultrahigh energy density, Nano Energy 39 (2017) 219–228.

[7] Q. Zhang, X. Wang, Z. Pan, J. Sun, J. Zhao, J. Zhang, et al., Wrapping aligned carbon nanotube composite sheets around vanadium nitride nanowire arrays for asymmetric coaxial fiber-shaped supercapacitors with ultrahigh energy density, Nano Lett. 17 (2017) 2719–2726.

[8] M. Winter, R.J. Brodd, What are batteries, fuel cells, and supercapacitors, Chem. Rev. 105 (2005), 1021-1021.

[9] A. Burke, Ultracapacitors: why, how, and where is the technology, J. Power Sources 91 (2000) 37–50.

[10] H. Chen, L. Hu, M. Chen, Y. Yan, L. Wu, Nickel-cobalt layered double hydroxide nanosheets for high-performance supercapacitor electrode materials, Adv. Funct. Mater. 24 (2014) 934–942.

[11] Y. Xiao, D. Su, X. Wang, S. Wu, L. Zhou, Z. Sun, Z. Wang, S. Fang, F. Li, Ultrahigh energy density and stable supercapacitor with 2D NiCoAl Layered double hydroxide, Electrochim. Acta 253 (2017) 324–332.

[12] C. Liu, F. Li, L.P. Ma, H.M. Cheng, Advanced materials for energy storage, Adv. Mater. 22 (2010) E28–E62.

[13] X. Lu, M. Yu, G. Wang, T. Zhai, S. Xie, Y. Ling, Y. Tong, Y. Li, H-TiO_2@ MnO_2//H-TiO_2@C core-shell nanowires for high performance and flexible asymmetric supercapacitors, Adv. Mater. 25 (2013) 267–272.

[14] L. Mai, X. Tian, X. Xu, L. Chang, L. Xu, Nanowire electrodes for electrochemical energy storage devices, Chem. Rev. 114 (2014) 11828–11862.

[15] Z. Tang, C.h. Tang, H. Gong, A high energy density asymmetric supercapacitor from nano-architectured $Ni(OH)_2$/Carbon nanotube electrodes, Adv. Funct. Mater. 22 (2012) 1272–1278.

[16] Y. Huang, Y. Zeng, M. Yu, P. Liu, Y. Tong, F. Cheng, et al., Recent smart methods for achieving high-energy asymmetric supercapacitors, Small Methods (2017) 1700230.

[17] Q. Wang, D. Hare, Recent advances in the synthesis and application of layered double hydroxide (LDH) nanosheets, Chem. Rev. 112 (2012) 4124–4155.

[18] G. Abellan, M. Latorre-Sanchez, V. Fornes, A. Ribera, H. García, Graphene as a carbon source effects the nanometallurgy of nickel in Ni, Mn layered double hydroxide-graphene oxide composites, Chem. Commun. 48 (2012) 11416–11418.

[19] L. Wang, D. Wang, X.Y. Dong, Z.J. Zhang, X.F. Pei, X.J. Chen, B. Chen, J. Jin, Layered assembly of graphene oxide and Co-Al layered double hydroxide nanosheets as electrode materials for supercapacitors, Chem. Commun 47 (2011) 3556–3558.

[20] Y. Liu, N. Fu, G. Zhang, M. Xu, W. Lu, L. Zhou, H. Huang, Design of hierarchical NiCo@NiCo layered double hydroxide core-shell structured nanotube Array for high-performance flexible all-solid-state battery-type supercapacitors, Adv. Funct. Mater. 27 (2017) 1605307.

[21] J. Zhao, J. Chen, S. Xu, M. Shao, D. Yan, M. Wei, D.G. Evans, X. Duan, CoMn-layered double hydroxide nanowalls supported on carbon fibers for high-performance flexible energy storage devices, J. Mater. Chem. A. 1 (2013) 8836–8843.

[22] A.D. Jagadale, G. Guan, X. Li, X. Du, X. Ma, X. Hao, A. Abudula, Ultrathin nanoflakes of cobalt-manganese layered double hydroxide with high reversibility for asymmetric supercapacitor, J. Power Sources 306 (2016) 526–534.

[23] X. Wu, L. Jiang, C. Long, T. Wei, Z. Fan, Dual support system ensuring porous Co-Al hydroxide nanosheets with ultrahigh rate performance and high energy density for supercapacitors, Adv. Funct. Mater. 25 (2015) 1648–1655.

[24] F. Ning, M. Shao, C. Zhang, S. Xu, M. Wei, X. Duan, Co_3O_4@ layered double hydroxide core/shell hierarchical nanowire arrays for enhanced supercapacitance performance, Nano Energy 7 (2014) 134–142.

[25] S. Wu, K. Hui, K. Hui, One-dimensional core-shell architecture composed of silver nanowire@hierarchical nickel-aluminum layered double hydroxide nanosheet as advanced electrode materials for pseudocapacitor, J. Phys. Chem. C 119 (2015) 23358–23365.

[26] J. Chen, X. Wang, J. Wang, P.S. Lee, Sulfidation of NiMn-layered double hydroxides/graphene oxide composites toward supercapacitor electrodes with enhanced performance, Adv. Energy Mater. 6 (2016) 1501745.

[27] J. Zhao, J. Chen, S. Xu, M. Shao, Q. Zhang, F. Wei, J. Ma, M. Wei, D.G. Evans, X. Duan, Hierarchical NiMn layered double hydroxide/carbon nanotubes architecture with superb energy density for flexible supercapacitors, Adv. Funct. Mater. 24 (2014) 2938–2946.

[28] J. Yang, C. Yu, X. Fan, Z. Ling, J. Qiu, Y. Gogotsi, Facile fabrication of MWCNT-doped NiCoAl-layered double hydroxide nanosheets with enhanced electrochemical performances, J. Mater. Chem. A. 1 (2013) 1963–1968.

[29] L. Lv, Z. Yang, K. Chen, C. Wang, Y. Xiong, 2D layered double hydroxides for oxygen evolution reaction: from fundamental design to application, Adv. Energy Mater. 9 (2019) 1803358.

[30] Y. Liu, X. Cao, L. Cui, Y. Zhong, R. Zheng, D. Wei, C. Barrow, J.M. Razal, W. Yang, J. Liu, Zn-Ni-Co trimetallic carbonate hydroxide nanothorns branched on $Cu(OH)_2$ nanorods array based on Cu foam for high-performance asymmetric supercapacitors, J. Power Sources 437 (2019) 226897.

[31] F. Liu, Y. Chen, Y. Liu, J. Bao, M. Han, Z. Dai, Integrating ultrathin and modified NiCoAl-layered double-hydroxide nanosheets with N-doped reduced

graphene oxide for high-performance all-solid-state supercapacitors, Nanoscale 11 (2019) 9896−9905.

[32] X. Cao, L. Cui, B. Liu, Y. Liu, D. Jia, W. Yang, J.M. Razal, J. Liu, Reverse synthesis of star anise-like cobalt doped Cu-MOF/$Cu_{2+1}O$ hybrid materials based on a $Cu(OH)_2$ precursor for high performance supercapacitors, J. Mater. Chem. A. 7 (2019) 3815−3827.

[33] Y. Liu, X. Cao, D. Jiang, D. Jia, J. Liu, Hierarchical CuO nanorod arrays in situ generated on three-dimensional copper foam via cyclic voltammetry oxidation for high-performance supercapacitors, J. Mater. Chem. A. 6 (2018) 10474−10483.

[34] T.T. Nguyen, J. Balamurugan, N.H. Kim, J.H. Lee, Hierarchical 3D Zn-Ni-P nanosheet arrays as an advanced electrode for high-performance all-solid-state asymmetric supercapacitors, J. Mater. Chem. A. 6 (2018) 8669−8681.

[35] Y. Wang, X. Lin, T. Liu, H. Chen, S. Chen, Z. Jiang, J. Liu, J. Huang, M. Liu, Wood-Derived hierarchically porous electrodes for high-performance all-solid-state supercapacitors, Adv. Funct. Mater. 28 (2018) 1806207.

[36] J.S. Valente, M. Sánchez-Cantú, E. Lima, F. Figueras, Method for large-scale production of multimetallic layered double hydroxides: formation mechanism discernment, Chem. Mater. 21 (2009) 5809−5818.

[37] P. Vialat, C. Mousty, C. Taviot-Gueho, G. Renaudin, H. Martinez, J.C. Dupin, E. Elkaim, F. Leroux, High-performing monometallic cobalt layered double hydroxide supercapacitor with defined local structure, Adv. Funct. Mater. 24 (2014) 4831−4842.

[38] F. Lai, Y.E. Miao, L. Zuo, H. Lu, Y. Huang, T. Liu, Biomass-Derived nitrogen-doped carbon nanofiber network: a facile template for decoration of ultrathin nickel-cobalt layered double hydroxide nanosheets as high-performance asymmetric supercapacitor electrode, Small 12 (2016) 3235−3244.

[39] T. Wang, S. Zhang, X. Yan, M. Lyu, L. Wang, J. Bell, H. Wang, 2-Methylimidazole-derived Ni-Co layered double hydroxide nanosheets as high rate capability and high energy density storage material in hybrid supercapacitors, ACS Appl. Mater. Interfaces 9 (2017) 15510−15524.

[40] K. Kan, L. Wang, P. Yu, B. Jiang, K. Shi, H. Fu, 2D quasi-ordered nitrogen-enriched porous carbon nanohybrids for high energy density supercapacitors, Nanoscale 8 (2016) 10166−10176.

[41] L. Yang, D. Liu, G. Cui, Y. Xie, $Cu_{2+1}O$/graphene nanosheets supported on three dimensional copper foam for sensitive and efficient non-enzymatic detection of glucose, RSC Adv. 7 (2017) 19312−19317.

[42] B. Li, T. Liu, L. Hu, Y. Wang, A facile one-pot synthesis of Cu_2O/RGO nanocomposite for removal of organic pollutant, J. Phys. Chem. Solid. 74 (2013) 635−640.

[43] E. Talik, M. Kruczek, W. Zarek, J. Kusz, K. Wojcik, H. Sakowska, W. Szyrski, XPS characterization of $YAlO_3$:Co single crystals, Cryst. Res. Technol.: J. Exp. Ind. Crystallogr 42 (2007) 1341−1347.

[44] C. Yuan, J. Li, L. Hou, X. Zhang, L. Shen, X.W. Lou, Ultrathin mesoporous $NiCo_2O_4$ nanosheets supported on Ni foam as advanced electrodes for supercapacitors, Adv. Funct. Mater. 22 (2012) 4592−4597.

[45] M. Shao, F. Ning, J. Zhao, M. Wei, D.G. Evans, X. Duan, Hierarchical layered double hydroxide microspheres with largely enhanced performance for ethanol electrooxidation, Adv. Funct. Mater. 23 (2013) 3513−3518.

[46] L. Xie, Z. Hu, C. Lv, G. Sun, J. Wang, Y. Li, H. He, J. Wang, K. Li, Co_xNi_{1-x} double hydroxide nanoparticles with ultrahigh specific capacitances as supercapacitor electrode materials, Electrochim. Acta 78 (2012) 205−211.

[47] X. Zhang, Y. Zhao, C. Xu, Surfactant dependent self-organization of Co_3O_4 nanowires on Ni foam for high performance supercapacitors: from nanowire microspheres to nanowire paddy fields, Nanoscale 6 (2014) 3638−3646.

[48] J. Liu, J. Jiang, C. Cheng, H. Li, J. Zhang, H. Gong, H.J. Fan, Co_3O_4 nanowire@MnO_2 ultrathin nanosheet core/shell arrays: a new class of high-performance pseudocapacitive materials, Adv. Mater. 23 (2011) 2076−2081.

[49] W. Tian, X. Wang, C. Zhi, T. Zhai, D. Liu, C. Zhang, D. Golberg, Y. Bando, $Ni(OH)_2$ nanosheet@Fe_2O_3 nanowire hybrid composite arrays for high-performance supercapacitor electrodes, Nano energy 2 (2013) 754−763.

[50] G. Hengzhi, B. Qing, S. Wu, O.K. Hui, Z. Erfan, Synthesis of hierarchical porous CuO Nanowire@NiCo-layered double hydroxide core-shell structured nanoarrays on copper foam for high-performance supercapacitors, J. Mater. Chem. (2017) 1−35.

[51] C. Schliehe, B.H. Juarez, M. Pelletier, S. Jander, D. Greshnykh, M. Nagel, A. Meyer, S. Foerster, A. Kornowski, C. Klinke, Ultrathin PbS sheets by two-dimensional oriented attachment, Science 329 (2010) 550−553.

[52] S. Gao, Y. Sun, F. Lei, L. Liang, J. Liu, W. Bi, B. Pan, Y. Xie, Ultrahigh energy density realized by a single-layer β-$Co(OH)_2$ all-solid-state asymmetric supercapacitor, Angew. Chem. Int. Ed. 53 (2014) 12789−12793.

[53] Q. Zhang, B. Zhao, J. Wang, C. Qu, H. Sun, K. Zhang, M. Liu, High-performance hybrid supercapacitors based on self-supported 3D ultrathin porous quaternary Zn-Ni-Al-Co oxide nanosheets, Nano Energy 28 (2016) 475−485.

[54] Y. Liu, X. Teng, Y. Mi, Z. Chen, A new architecture design of Ni-Co LDH-based pseudocapacitors, J. Mater. Chem. A. 5 (2017) 24407−24415.

[55] L. Li, J. Fu, K. San Hui, K.N. Hui, Y.-R. Cho, Controllable preparation of 2D nickel aluminum layered double hydroxide nanoplates for high-performance supercapacitors, J. Mater. Sci. Mater. Electron. 29 (2018) 17493−17502.

[56] L. Zhang, H. Yao, Z. Li, P. Sun, F. Liu, C. Dong, J. Wang, Z. Li, M. Wu, C. Zhang, Synthesis of delaminated layered double hydroxides and their assembly with graphene oxide for supercapacitor application, J. Alloys Compd. 711 (2017) 31−41.

[57] S. Wang, Z. Huang, R. Li, X. Zheng, F. Lu, T. He, Template-assisted synthesis of NiP@CoAl-LDH nanotube arrays with superior electrochemical performance for supercapacitors, Electrochim. Acta 204 (2016) 160−168.

[58] J. Xing, J. Du, X. Zhang, Y. Shao, T. Zhang, C. Xu, A Ni-P@NiCo LDH core-shell nanorod-decorated nickel foam with enhanced areal specific capacitance for high-performance supercapacitors, Dalton Trans. 46 (2017) 10064−10072.

[59] P. Wang, Y. Li, S. Li, X. Liao, S. Sun, Water-promoted zeolitic imidazolate framework-67 transformation to Ni-Co layered double hydroxide hollow microsphere for supercapacitor electrode material, J. Mater. Sci. Mater. Electron. 28 (2017) 9221−9227.

[60] T. Liang, H. Xuan, Y. Xu, J. Gao, X. Han, J. Yang, P. Han, D. Wang, Y. Du, Rational assembly of CoAl-layered double hydroxide on reduced graphene oxide with enhanced electrochemical performance for energy storage, ChemElectroChem 5 (2018) 2424−2434.